JACS
JOURNAL OF THE AMERICAN CHEMICAL SOCIETY
Article
pubs.acs.org/JACS

L-Edge X-ray Absorption Spectroscopic Investigation of {FeNO}^{6}: Delocalization vs Antiferromagnetic Coupling

James J. Yan,[†] Margarita A. Gonzales,[‖] Pradip K. Mascharak,*[,§] Britt Hedman,*[,‡] Keith O. Hodgson,*[,†,‡] and Edward I. Solomon*[,†,‡]

[†]Department of Chemistry, Stanford University, Stanford, California 94305, United States
[‖]Department of Chemistry, Foothill College, Los Altos Hills, California 94022, United States
[§]Department of Chemistry and Biochemistry, University of California, Santa Cruz, California 95064, United States
[‡]Stanford Synchrotron Radiation Lightsource, SLAC National Accelerator Laboratory, Stanford University, Menlo Park, California 94025, United States

Supporting Information

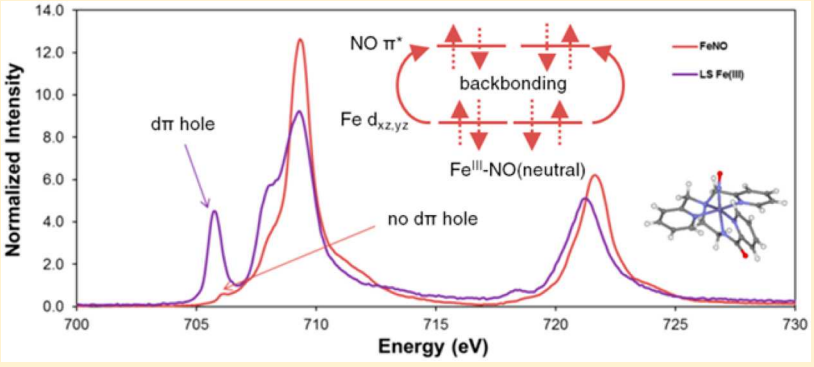

ABSTRACT: NO is a classic non-innocent ligand, and iron nitrosyls can have different electronic structure descriptions depending on their spin state and coordination environment. These highly covalent ligands are found in metalloproteins and are also used as models for Fe−O_2 systems. This study utilizes iron L-edge X-ray absorption spectroscopy (XAS), interpreted using a valence bond configuration interaction multiplet model, to directly experimentally probe the electronic structure of the S = 0 {FeNO}^{6} compound [Fe(PaPy$_3$)NO]$^{2+}$ (PaPy$_3$ = *N*,*N*-bis(2-pyridylmethyl)amine-*N*-ethyl-2-pyridine-2-carboxamide) and the S = 0 [Fe(PaPy$_3$)CO]$^+$ reference compound. This method allows separation of the σ-donation and π-acceptor interactions of the ligand through ligand-to-metal and metal-to-ligand charge-transfer mixing pathways. The analysis shows that the {FeNO}^{6} electronic structure is best described as Fe^{III}−NO(neutral), with no localized electron in an NO π^* orbital or electron hole in an Fe dπ orbital. This delocalization comes from the large energy gap between the Fe−NO π-bonding and antibonding molecular orbitals relative to the exchange interactions between electrons in these orbitals. This study demonstrates the utility of L-edge XAS in experimentally defining highly delocalized electronic structures.

1. INTRODUCTION

The electronic structure of highly covalent iron systems can be difficult to determine with traditional spectroscopic methods.[1] Certain ligands, such as O_2,[2−8] and NO,[9−13] allow for significant delocalization of electrons between the Fe 3d orbitals and the ligand π^* orbitals. This delocalization can lead to multiple possible electronic structure descriptions, which can include antiferromagnetic coupling between electrons on the metal and on the ligand. Low-spin (S = 0) {FeNO}^{6} complexes (using the Enemark-Feltham nomenclature, where the superscript denotes the number of electrons shared between the Fe 3d and ligand π^* valence orbitals[14]) are an important class of such systems. In different biological systems[11,15−17] FeNO has been used as a stable analogue of FeO_2 for study.[18,19] Additionally, {FeNO}^{6} model compounds have been synthesized with photolabile Fe−NO bonds that have potential in photodynamic therapies.[20−22] This photolability is interesting as the Fe-(NO) bond is short and has been shown to involve a potential energy surface crossing as the bond elongates.[23] Early Mössbauer studies suggested an antiferromagnetically coupled Fe^{IV} (S = 1)−NO$^-$ (S = −1) electronic structure.[24] More recent DFT and Mössbauer, absorption, and vibrational spectroscopic studies have suggested a Fe^{II}−NO$^+$ electronic structure.[22,25,26] Oriented single-crystal nuclear resonance vibrational and IR spectroscopy on a five- and six-coordinate [Fe(OEP)NO]$^+$ were also consistent with formally Fe^{II}−NO$^+$, but the Mössbauer isomer shifts on the same compounds were more

Received: October 28, 2016
Published: December 22, 2016

DOI: 10.1021/jacs.6b11260
J. Am. Chem. Soc. 2017, 139, 1215−1225

similar to Fe^{IV}.[27] Sulfur K-edge X-ray absorption spectroscopy (XAS) also suggested a $Fe^{II}-NO^{+}$ electronic structure, but with strong backbonding from the metal leading to an effective nuclear charge on the Fe, Z_{eff}, closer to Fe^{III},[11] similar to the assignment from vibrational spectroscopy on $[Fe(TPP)(MI)NO]^{+}$.[23] The present study uses L-edge XAS to directly experimentally determine the electronic structure of a structurally defined 6C $S = 0$ $\{FeNO\}^6$ model compound.

L-edge XAS is a very effective tool for studying iron centers in highly covalent systems.[1,28,29] The L-edge experiment involves an electric dipole-allowed 2p→3d transition, which provides a direct probe of the unoccupied and partially occupied metal 3d orbitals.[30] The transitions produce $2p^5 3d^{N+1}$ final states that are energy split by p-d and d-d electron repulsion, ligand field effects, and spin-obit coupling (SOC) to produce multiplets that make up the L-edge XAS spectrum. The 2p core hole has a large SOC constant, splitting the L-edge into two regions, the L_3 ($J = 3/2$) edge and the L_2 ($J = 1/2$) edge. These are split by ∼10−15 eV, with the L_3 at lower energy and an L_3/L_2 intensity ratio of ∼2:1. Due to the localized nature of the Fe 2p orbital, the 2p→3d transition is localized on the iron center and the intensity of the L-edge is directly proportional to the amount of metal d-character in the valence orbitals. As the amount of metal d-character in unoccupied orbitals increases, the total L-edge intensity increases, and vice versa. Ligand donor interactions lead to a decrease in the d-character, and decrease in L-edge intensity. This is covalent donor bonding that can be described by mixing ligand character into the metal valence orbitals through ligand-to-metal charge-transfer (LMCT) configuration interaction (CI). Conversely backbonding, which can be described by metal-to-ligand charge-transfer (MLCT) mixing, increases the L-edge intensity by mixing occupied metal dπ-character into unoccupied ligand orbitals. Our previous studies have shown that this mixing leads to a new, high-energy peak in the L-edge spectrum that is not present for analogous systems without MLCT mixing (i.e., backbonding).[31]

In D_{4h} symmetry, the ligand field splits the 3d orbitals into different symmetry sets. Because the orbitals have different symmetry, the LMCT and MLCT CI affect the orbitals differently, leading to differential orbital covalency (DOC) (i.e., different bonding interactions for each symmetry set of d orbitals). Through multiplet modeling of the experimental spectrum, the DOC of the system can be extracted. This allows for the differentiation between dσ and dπ donation,[32] and for separation of the LMCT and MLCT contributions, the latter quantifying the π-acceptor ability of the ligand.[31] The L-edge XAS/DOC methodology is therefore a powerful tool for studying highly covalent systems and allows for a detailed experimental definition of their electronic structure. This methodology has been applied to various heme[1] and non-heme[28,30−32] systems previously, including a heme $\{FeO_2\}^8$ system.[29] The present study applies this L-edge XAS/DOC methodology to the structurally defined low-spin ($S = 0$) ferrous complex, $[Fe(PaPy_3)CO]^{+}$ (FeCO),[33] and its complementary $S = 0$ $\{FeNO\}^6$ complex, $[Fe(PaPy_3)NO]^{2+}$ (FeNO),[22] to experimentally determine the electronic structures of the nitrosyl using the carbonyl as a well-defined reference having low-spin Fe^{II} with some backbonding into the carbonyl. Their structures are shown in Figure 1. For the $\{FeNO\}^6$ $S = 0$ model, an interesting electronic structure description arises which is highly relevant to $S = 0$ $\{FeO_2\}^8$ complexes including oxyhemoglobin. The electronic structure

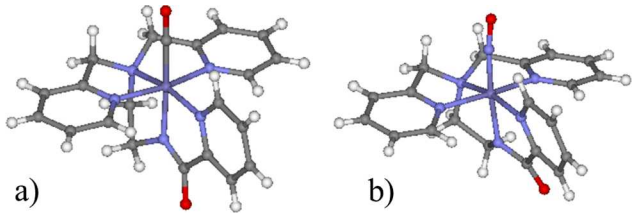

Figure 1. Crystal structures of (a) FeCO[33] and (b) FeNO.[22] Purple = Fe, red = O, blue = N, gray = C, white = H.

description of oxyhemoglobin has been the subject of continued discussion, mostly based on calculations; the descriptions include unpolarized (i.e., $S = 0$ $Fe^{II}/{}^1O_2$)[2,3] and polarized ($S = 1$ $Fe^{II}/{}^3O_2$) $Fe^{II}-O_2$,[5−8] and polarized, antiferromagnetically coupled $Fe^{III}-O_z^{-4}$ electronic structures. The present study deals with these issues for $\{FeNO\}^6$ and elucidates the interactions responsible for electron delocalization with and without magnetic coupling.

2. MATERIALS AND METHODS

2.1. Samples. The compounds $[Fe(PaPy_3)CO]^{+}$ and $[Fe(PaPy_3)NO]^{2+}$ were synthesized and characterized according to published methods.[22,33] Prior to data collection, all samples were stored in a −80 °C freezer. For the L-edge measurements, the samples were spread across double-sided adhesive conductive graphite tape and attached to a copper paddle in a nitrogen glovebag. For the $[Fe(PaPy_3)NO]^{2+}$ sample, the loading of the sample onto the copper paddle was performed in the dark, except for a single red light, to minimize photolysis of the Fe−NO bond. The samples were transferred to a separate nitrogen glovebag for loading into the ultra-high-vacuum (UHV) experimental chamber (to which this glovebag was attached). The copper paddle containing the $[Fe(PaPy_3)NO]^{2+}$ sample was transferred in a sealed container wrapped in aluminum foil to prevent photodamage.

2.2. XAS Data Collection and Reduction. X-ray absorption spectra were collected at the Stanford Synchrotron Radiation Lightsource on the 31-pole wiggler beamline 10-1 under ring operating conditions of 350 mA and 3 GeV. The radiation was dispersed using a spherical grating monochromator set at 1000 lines/mm with 20 μm entrance and exit slits for a resolution of ∼0.1 eV. Data for both samples were recorded using a UHV beamline end-station chamber maintained at 5.0×10^{-9} Torr with samples aligned normal to the incident beam.

L-edge spectra were measured by total electron yield with a Galileo 4716 channeltron electron multiplier aligned 45° relative to the incident beam. The sample signal (I_1) was normalized (I_1/I_0) by the photocurrent of an upstream gold-grid reference monitor (I_0). The photon energy was calibrated to 708.5 and 720.1 eV for the maximum of the L_3-edge and lower-energy feature of the L_2-edge, respectively, of powdered α-Fe_2O_3 (hematite <5 μM) run before and after each set of sample scans. Data were collected over the range of 670−830 eV to allow for proper normalization with a step size of 0.1 eV employed from 700 to 730 eV, and 0.5 eV for remaining regions of the spectrum.[30]

To minimize sample decay from vacuum pumping, samples were precooled in an antechamber with a liquid nitrogen coldfinger before exposure to vacuum, and then loaded onto a chamber cryostat, which was precooled to 220−240 K. Pumping was minimized by rapid transfer into the experimental chamber. All windows on the chamber were covered with aluminum foil when measuring the $[Fe(PaPy_3)NO]^{2+}$ sample to prevent visible light photodamage. A single scan of the L-edge spectrum lasted an average of ∼10 min, with ∼4 min over the 700−730 eV energy region. Both samples displayed gradual photodamage from exposure to the X-ray beam. Maintaining the samples at lower temperature reduced the rate of decay from pumping and photodamage. Multiple scans of the samples were done to minimize decay and ensure reproducibility of the data.

DOI: 10.1021/jacs.6b11260
J. Am. Chem. Soc. 2017, 139, 1215−1225

A linear background function was first subtracted from each data set, to which two arctangent functions of the form absorption (χ) = $\{\tan^{-1}[k(\text{energy} - I_1) + \pi/2](2/3)(1/\pi)\} + \{(\tan^{-1}[k(\text{energy} - I_2) + \pi/2](1/3)(1/\pi))\}$, with k = 0.295, obtained by experimental fit,[30,34] and $I_2 = I_1 + 12.3$ eV (energy split by spin−orbit coupling), were used to model the L_3- and L_2-edge jumps with each set normalized to 1.0 at 830 eV, as done previously.[27] The energy of the arctangent was estimated on the basis of the fit to the L-edge experiment. For the $[Fe(PaPy_3)CO]^+$ sample, which exhibited significant degradation due to pumping, the data set was corrected by subtracting a percentage of the five-coordinate pumped control sample spectrum, followed by renormalization, as described previously.[30] For the $[Fe(PaPy_3)NO]^{2+}$ sample, there was little effect of pumping, but degradation due to X-ray photodamage was found. This was corrected by performing 16 consecutive scans on the same sample spot to monitor the photodamage and then extrapolating the amount of damage in the sample scans based on the rate of growth of features caused by photodamage. The amount of decay in the XAS data presented is <5%.

The total intensity reported here is the combined area of the L_3 and L_2 intensities and is calculated after normalization over the ranges of 700−715 and 715−730 eV, respectively. The error reported represents the range of integrated L-edge intensities based on repeat measurements of the same spectrum, on different dates, and on multiple samples.

2.3. Valence Bond Configuration Interaction (VBCI) Multiplet Simulations. Ligand field multiplet calculations were performed using the multiplet model implemented by Thole,[35] with the atomic theory developed by Cowan,[36] and the crystal field symmetry interactions described by Butler,[37] which includes both Coulomb interactions and spin−orbit coupling for each subshell.[38,39] To simulate the spectra, the Slater−Condon−Shortley parameters F_l and G_l were reduced to 80% of their Hartree−Fock calculated values in order to account for the overestimation of electron−electron repulsion found in the calculations of the free ion (κ = 0.8).[38,40,41] The final multiplet spectrum is calculated from the sum of all transitions for electrons excited from an Fe 2p orbital into the 3d unoccupied orbitals.[42] In the ligand field limit, the ground state is approximated by a single electronic configuration d^N split in energy by a ligand field potential in D_{4h} symmetry, which is defined by the parameters 10Dq, Ds, and Dt. The FeCO and FeNO complexes are treated as being effectively D_{4h} symmetry due to the relatively short axial bond lengths relative to the equatorial bond lengths (see Table 4, below). The relationships between orbital energies and ligand field parameters are b_{1g} ($d_{x^2-y^2}$) = 6Dq + 2Ds − 1Dt, a_{1g} (d_{z^2}) = 6Dq − 2Ds − 6Dt, b_{2g} (d_{xy}) = −4Dq + 2Ds − 1Dt, and e_g ($d_{xz/yz}$) = −4Dq − 1Ds + 4Dt. Covalent mixing of the valence metal d orbitals with the valence ligand p orbitals was included using a charge transfer configuration interaction model in which LMCT adds a $d^{N+1}\underline{L}$ configuration ($\underline{L}$ = ligand hole) at an energy (Δ) above the d^N ground state. These two states couple through CI, which is introduced by the mixing term $T_i = \langle 3d^N|h|3d^{N+1}\underline{L}\rangle$, where h is the molecular Hamiltonian operator and T_i is proportional to the metal−ligand overlap for each of the i symmetry blocks. In the case of a donor ligand system, the ground state is defined by $\Psi_{GS,B} = \alpha_1|3d^N\rangle + \beta_1|3d^{N+1}\underline{L}\rangle$, the LMCT state is defined by $\Psi_{GS,AB} = \beta_1|3d^N\rangle - \alpha_1|3d^{N+1}\underline{L}\rangle$, and the corresponding excited states are defined as $\Psi_{ES,B} = \alpha_2|2p^53d^{N+1}\rangle + \beta_2|2p^53d^{N+2}\underline{L}\rangle$, and $\Psi_{ES,AB} = \beta_2|2p^53d^{N+1}\rangle - \alpha_2|2p^53d^{N+2}\underline{L}\rangle$. Here the coefficients α_1, α_2, β_1, and β_2 are functions of T and Δ for the ground state and T and Δ' for the final state, where $\Delta' = \Delta + U - Q$, where U is the 3d-3d electron repulsion and Q is the 2p-3d repulsion. To limit the number of variables, $Q - U$ was maintained at 1.0 eV.[43] Additionally, the ligand field parameters (10Dq, Ds, and Dt), T, and Δ were fixed in the ground and final state. MLCT was included by introduction of a third configuration defined as $d^{N-1}L^-$, separated from the ground state by an energy, Δ_{bb} (Δ-backbonding). The resultant ground-state wave functions are thus combinations of three configurations, $3d^{N-1}L^-$, $3d^N$, and $3d^{N+1}\underline{L}$.[31]

To simulate the L-edge spectra, parameters were initially chosen on the basis of the carbonyl reference compound[28] and constraints obtained from density functional theory (DFT) results (*vide infra*). The energy separations between the $d^{N-1}L^-$, d^N, and $d^{N+1}\underline{L}$ configurations in the ground state (Δ and Δ_{bb}) were obtained from the program parameters. In the multiplet program, the parameters EG1, EG2, and EG3 represent the ground state energies of the $d^{N-1}L^-$, d^N, and $d^{N+1}\underline{L}$ configurations, respectively, and are defined as EG1 = 0, EG2 = $-\Delta_{bb}$, and EG3 = $\Delta - \Delta_{bb}$. The parameters for the final state energies of the configurations are EF1, EF2, and EF3, respectively, and are defined as EF1 = 0, EF2 = $-\Delta_{bb} - (Q - U)$, and EF3 = $\Delta - \Delta_{bb} - 2(Q - U)$.

In order to obtain covalency values for each of the symmetry blocks, a DOC projection method was applied that uses the multiplets[30] to distribute the intensity into its different symmetry components via virtual 4s→5s transitions. These projected values were degeneracy weighted and calibrated to the experimental total intensity to extract the DOC. The final simulated fit to each spectrum was evaluated on the basis of simulated spectral shape relative to the data, the relative weights of the three ground configurations ($d^{N-1}L^-$, d^N, and $d^{N+1}\underline{L}$), the projected intensities into each of the symmetry blocks, and its agreement with other spectroscopic and computational results.

2.4. DFT Calculations. The starting structures for the compounds were taken directly from their crystal structures.[22,33] Ground-state DFT calculations and geometry optimizations were performed with Gaussian 09[44] using three different unrestricted functionals (BP86,[45,46] B3LYP,[47,48] and BP86 + 40% HF) with the 6-311G* basis set. Frequency calculations on the final optimized geometries contained only real frequencies. Mulliken populations were analyzed using QMForge.[49]

3. RESULTS AND ANALYSIS

3.1. L-Edge XAS. L-edge X-ray absorption spectroscopic data were collected on the S = 0 compounds $[Fe(PaPy_3)NO]^{2+}\{FeNO\}^6$(FeNO) and $[Fe(PaPy_3)CO]^+$(FeCO) under UHV with electron yield detection. The L-edge spectrum of FeNO (Figure 2B) shows a similar shape to the previously studied S = 0 Fe(II)$(tacn)_2$ spectrum[27] (Figure 2C), displaying a single peak in the L_3 and L_2 edges at 709.3 and 721.6 eV, respectively. In contrast to the spectrum[30] of low-spin

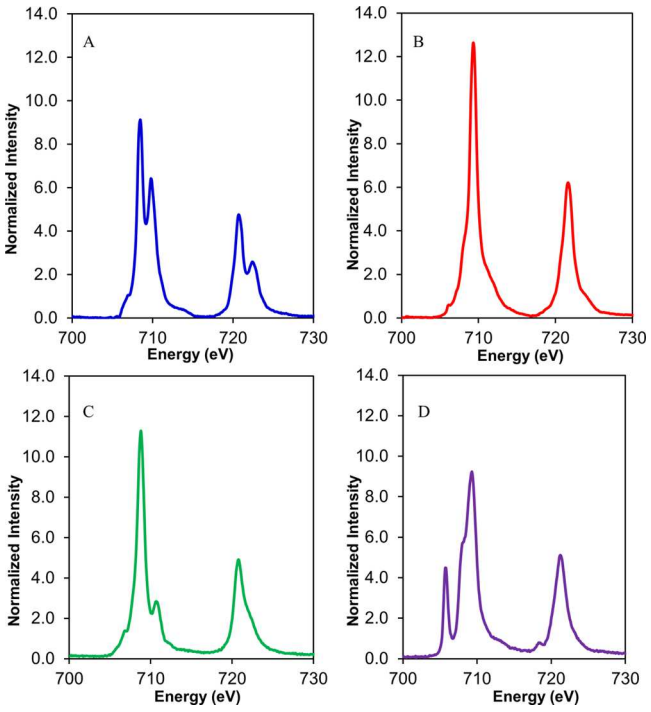

Figure 2. Fe L-edge spectra for (A) low-spin ferrous $[Fe(PaPy_3)CO]^+$, (B) S = 0 $[Fe(PaPy_3)NO]^{2+}\{FeNO\}^6$, (C) low-spin ferrous $Fe(tacn)_2$, and (D) low-spin ferric $[Fe(tacn)_2]Cl$.

DOI: 10.1021/jacs.6b11260
J. Am. Chem. Soc. 2017, 139, 1215−1225

Fe(III)(tacn)$_2$ (Figure 2D), the spectrum of FeNO does not show a sharp low-energy peak indicative of a dπ hole of a low-spin Fe(III) spectrum (at ~706 eV in Fe(III)(tacn)$_2$). The total integrated intensity of the FeNO spectrum is 41 normalized units for a total metal d-character of 334% in the unoccupied valence orbitals.[30] The integrated intensity for a low-spin Fe(III) is 44, while that for a low-spin Fe(II) is 37 (Table 1).

Table 1. Summary of Iron L-Edge Experimental Data[a]

compound	total intensity	total % metal character	L_3, L_2 maxima
$[Fe(PaPy_3)CO]^+$	36(6)	286	708.5, 720.7
$[Fe(PaPy_3)NO]^{2+}$	41(5)	334	709.3, 721.6
$Fe^{II}(tacn)_2$	37(5)	288	708.8, 720.8
$[Fe^{III}(tacn)_2]Cl$	44(5)	351	709.3, 721.2

[a]The total percent metal character represents the amount of d-character in the unoccupied orbitals and includes the effects of covalency and backbonding. Maxima are given in eV at the energy of the L_3- and L_2-edges.

The spectrum of this FeNO thus has an intensity between that of Fe(II) and Fe(III) but somewhat closer to that of Fe(III), even without the intensity associated with the dπ hole.

The L-edge spectrum of the low-spin ferrous reference compound, FeCO (Figure 2A), shows very different features compared to the FeNO spectrum. While the FeNO L_3 edge shows a single intense peak at 709.3 eV, the FeCO L_3 edge shows two distinct and less intense peaks with the main peak at 708.5 eV and a smaller peak at 709.8 eV. The L_2 edge shows a similar double peak pattern, with peak energies of 720.7 and 722.4 eV. As shown in our previous study on $[Fe(CN)_6]^{2-}$,[31] the double peak pattern is due to filled metal 3d orbitals backbonding into empty ligand (CN^-, CO) π^* orbitals. The total integrated intensity of the FeCO spectrum is 36 normalized units, significantly less than the normalized intensity of the FeNO spectrum, but comparable to that of the low-spin Fe(II) with no backbonding.

The lower intensity of the FeCO spectrum compared to that of the FeNO spectrum could have two origins. One possibility is that the FeNO compound is overall less covalent than the FeCO compound. The other possibility is that NO is a better backbonding ligand than CO. Since NO also has empty π^* orbitals for backbonding and since in the crystal structures the Fe−NO bond length (1.68 Å) is shorter than the Fe−CO bond length (1.77 Å), the backbonding explanation is more plausible. However, FeNO does not display the double peak pattern of a backbonding ligand that is present, for example, in the FeCO spectrum in Figure 2A. But, as the NO π^* comes down in energy, the two peaks can merge.[29,31] This is investigated further in the next section.

3.2. VBCI Analysis of L-Edge Data. VBCI modeling was used to further analyze the experimental L-edge spectra. The FeCO spectrum was fit first, through an iterative approach, changing the ligand field (10Dq, Ds, Dt), T, and Δ parameters. The fit of the FeCO spectrum was then used as a starting point for fitting the FeNO spectrum, due to the similarity in the ligand sets. The final multiplet fits are presented in Figure 3 (FeCO) and Figure 4 (FeNO) and the fit parameters are given in Table 2. The FeCO spectrum was successfully fit by including both LMCT (i.e., σ and π donation) and MLCT (π backbonding) configurations; the latter gives the backbonding into the π^* orbital of the CO ligand. While the simulation over

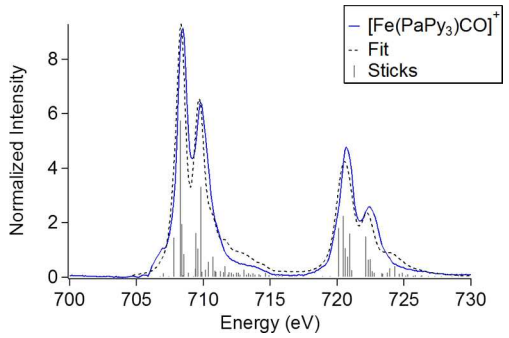

Figure 3. Final VBCI fit (---) for low-spin ferrous $[Fe(PaPy_3)CO]^+$. The sticks represent the individual multiplet transitions that contribute to the simulated spectrum. Broadening introduced by convolution of a Gaussian function (σ = 0.2 eV) and a Lorentzian function (half-width = 0.2 eV from 700 to 718 and 0.4 eV from 718 to 730 eV) to represent instrument and lifetime broadening, respectively. The VBCI fit reproduces the feature at 709.8 eV associated with backbonding into the CO π^* orbitals.

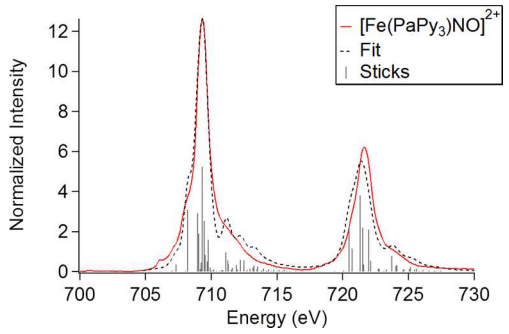

Figure 4. Final VBCI fit (---) for $[Fe(PaPy_3)NO]^{2+}\{FeNO\}^6$. The sticks represent the individual multiplet transitions that contribute to the simulated spectrum. The VBCI fit reproduces the merging of the backbonding peak with the main peak.

predicts the intensity at the higher energy tail (~712 eV L_3, ~724 eV L_2), a comparison of the fits for FeCO and FeNO reproduce the experimental trend showing lower intensity in that region for FeCO than FeNO (Figure S1). The projected differential orbital covalencies (DOC) from the fit were 43%, 68%, and 16% metal character in the d_{z^2}, $d_{x^2-y^2}$, and CO π^* orbitals, respectively (Table 3). The difference in covalency between the σ-bonding orbitals reflects the much shorter axial bonds compared to the equatorial bonds in FeCO (1.86 Å average axial bond length vs 1.99 Å average equatorial bond length). The π backbonding is somewhat less compared to the previously studied $[Fe^{II}(pfp)(1\text{-MeIm})CO]$ complex[26] (16% vs 20%), However, the 20% backbonding of $[Fe^{II}(pfp)(1\text{-MeIm})CO]$ includes backbonding into the porphyrin as well as into the CO ligand.

Simulations of backbonding in Fe compounds (Figure 5) show that as the Δ_{bb} becomes more negative (bottom to top in Figure 5) in a low-spin ferrous system (i.e., as the π^* orbital comes down in energy), the backbonding peak moves closer to the main peak and eventually becomes a new low-energy dπ hole peak that is characteristic of a low-spin ferric complex (top in Figure 5 as in Figure 2D for $Fe^{III}(tacn)_2$). In the intermediate region ($\Delta_{bb} \approx -3$ eV), the backbonding peak has merged with the main peak to form a single feature.

Since the difference between the CO and NO compounds considered here is in the axial ligand and its backbonding

DOI: 10.1021/jacs.6b11260
J. Am. Chem. Soc. 2017, 139, 1215−1225

Table 2. Final VBCI Fit Parameters[a]

	crystal field	configuration energies			mixing parameters (T)		
compound	10Dq, Ds, Dt	Δ	Δ_{bb}	$Q-U$	x^2-y^2 (b_{1g})	z^2 (a_{1g})	xz/yz (π^*)
$[Fe(PaPy_3)CO]^+$	2.65, 0.08, −0.12	−4.0	−2.0	1.0	1.1	1.6	1.3
$[Fe(PaPy_3)NO]^{2+}$	2.70, −0.03, −0.07	−3.1	−3.9	1.0	1.6	2.5	1.3

[a]Final fit parameters for the $2p^6$ initial state and the $2p^5$ final state with a d^6 ground-state configuration. b_{1g} and a_{1g} represent LMCT mixing parameters, and π^* represents MLCT mixing. All other T values were set to zero.

Table 3. Comparison of Calculated and Experimental d Characters in Unoccupied Valence Orbitals

	total % metal d character		VBCI (DFT) % metal character per orbital (DOC)			
compound	VBCI	DFT	x^2-y^2 (b_{1g})	z^2 (a_{1g})	$xz/yz/xy$ (t_{2g})	xz/yz (π^*)
$[Fe(PaPy_3)CO]^+$	286	276	68 (64)	43 (50)		16 (12)
$[Fe(PaPy_3)NO]^{2+}$	334	342	69 (64)	50 (51)		24 (28)
$Fe^{II}(tacn)_2$	288	284	72 (71)	72 (71)		
$[Fe^{III}(tacn)_2]Cl$	351	341	63 (62)	63 (62)	99 (93)	

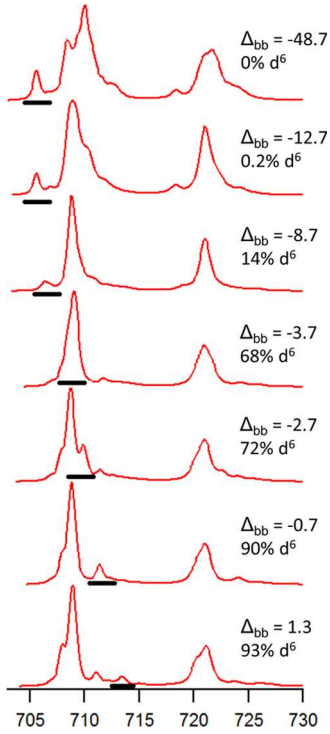

Figure 5. Set of simulations including both LMCT and MLCT configurations. Δ_{bb} was varied while all T and crystal field parameters were fixed. The position of the backbonding peak, denoted by the black bar, moves to lower energy as Δ_{bb} becomes more negative and becomes the Fe^{III} dπ hole at the top.

capability, the iterative fitting process in fitting FeNO starting from FeCO first focused on varying the MLCT parameters, and then the LMCT and ligand field parameters. The FeNO spectrum was successfully fit using the same three-configuration model used for the CO complex that includes both LMCT and MLCT, starting from the Fe(II)−NO^+ limit. In the final fit parameters used to fit the FeNO data in Figure 4, the Δ_{MLCT} decreases from −2.0 in the FeCO complex to −3.9 in the FeNO complex, demonstrating that the ligand π^* manifold is lower in energy by ∼2 eV in the FeNO relative to the FeCO complex. While the Δ_{LMCT} and LMCT T (i.e., charge transfer ener and ligand−metal overlap, respectively) parameters change between the CO and NO complexes, the T_{a1g} parameter (i.e., d_{z^2} overlap) remains higher than the T_{b1g} parameter (i.e., $d_{x^2-y^2}$ overlap) in both, showing that both FeCO and FeNO have a large difference in covalency between the d_{z^2} and $d_{x^2-y^2}$ orbitals. The projected DOC for FeNO complex gives covalencies of 50%, 69%, and 24% metal character in the d_{z^2}, $d_{x^2-y^2}$, and NO π^* orbitals, respectively (Table 3). Compared to the FeCO complex, the FeNO complex has a less covalent d_{z^2} orbital (50% vs 43%) while having a similar covalency in the $d_{x^2-y^2}$ orbital (69% vs 68%), reflecting the difference in σ-bonding between the NO and CO ligands and the similarity in bonding of the $PaPy_3$ ligand.

The major difference between the spectra in Figure 2A,B comes from the backbonding, where the FeNO complex shows a much greater amount of backbonding than FeCO (24% vs 16%). The much stronger π backbonding in FeNO explains why the Fe−NO bond length (1.68 Å) is shorter than the Fe−CO bond length (1.77 Å), despite the NO ligand having less σ covalency than the CO ligand. The DOC shows that the difference in covalency between the two compounds is due primarily to the difference in backbonding, with the NO ligand having a lower energy π^* set of orbitals. The VBCI modeling also shows that this lower energy MLCT configuration leads to the merging of the double peak feature in the FeCO complex in Figure 2A, characteristic of backbonding ligands, into a single peak, as observed experimentally in Figure 2B. Additionally, the total amount of backbonding metal 3d character among the four unoccupied holes in the NO π^* orbitals is 96%. This amount is very similar to the unoccupied 3d character in the t_{2g} hole of $Fe(III)(tacn)_2$ (99%, Table 3), demonstrating that the formally low-spin Fe(II) has backbonded enough metal character into the NO π^* orbitals to be best described as having the Z_{eff} of Fe(III). However, there is no dπ hole peak as found in the L-edge of low-spin Fe(III) complexes (Figure 2D). Thus, the electronic structure of the FeNO complex is best described as an Fe(III)−NO(neutral), where the electron density, as shown through the VBCI fitting, is delocalized among the four unoccupied orbitals of the NO π^* to give NO(neutral), rather than localized in a single orbital as in the $NO^\bullet$ radical.

3.3. DFT Calculations. Calculations were performed on both the FeCO and FeNO complexes starting from their crystal structures. Geometry optimizations using the BP86 functional did not appreciably alter these geometries (Table 4). The calculated covalencies for the compounds also agree with the covalencies projected through the VBCI modeling (Table 3). For the FeCO compound, the total calculated unoccupied d

DOI: 10.1021/jacs.6b11260
J. Am. Chem. Soc. 2017, 139, 1215−1225

Table 4. Geometric Parameters of Compounds[a]

compound	Fe axial (Å)	Fe−C/N−O angle (deg)	Fe transaxial (Å)	Fe equatorial (Å)
$[Fe(PaPy_3)CO]^+$ crystal	1.77	176.6	1.94	1.99
$[Fe(PaPy_3)CO]^+$ BP86	1.77	177.2	1.94	1.99
$[Fe(PaPy_3)NO]^{2+}$ crystal	1.68	173.1	1.90	1.98
$[Fe(PaPy_3)NO]^{2+}$ BP86	1.67	171.4	1.89	2.01
$[Fe(PaPy_3)NO]^{2+}$ B3LYP	1.71	169.0	1.87	2.02
$[Fe(PaPy_3)NO]^{2+}$ 40% HF	1.99	143.2	1.79	1.98

[a]Crystal structure and calculated bond lengths. The equatorial bond lengths represent the average of four equatorial ligands. All calculations were done in Gaussian 09 with the 6-311G* basis set. The 40% HF functional is a hybrid functional of BP86 mixed with 40% Hartree−Fock. The B3LYP and 40% HF calculations are spin-polarized.

character (276) is similar to the experimental unoccupied d character (286). The calculated electronic structure was less covalent in the d_{z^2} orbital (50% vs 43%) and in the backbonding orbitals (12% vs 16%), while the calculated $d_{x^2-y^2}$ orbital was more covalent (64% vs 68%). In the calculated molecular orbital energy diagram (Figure 6 left, blue), the metal d_{z^2} orbital is higher in energy than the $d_{x^2-y^2}$ orbital, reflecting the stronger axial bonding compared to equatorial bonding. The CO π^* orbitals are also higher in energy than all the metal d orbitals, reflecting the high-energy backbonding peak seen in the experimental L-edge spectrum in Figure 2B at 709.8 eV.

For the FeNO compound, the calculated unoccupied d character (342) is also very similar to the experimental value from integrated intensity (334, Table 3). Like the FeCO compound, the calculated d_{z^2} orbital was a bit less covalent (51% vs 50%) and the calculated $d_{x^2-y^2}$ orbital was more covalent (64% vs 69%); however the NO π^* backbonding orbitals were calculated to be more covalent (28% vs 24% d character), and can be seen in Figure 7 (top). DFT calculations on $[Fe(TPP)(MI)NO]^+$ showed comparable amounts of backbonding in that system as well.[23] Similar to the FeCO calculations, the calculated FeNO metal d_{z^2} orbital is higher in energy than the $d_{x^2-y^2}$ orbital for the FeNO compound (Figure 6, second column, red). Importantly, the calculated NO π^* orbitals are now lower in energy than the unoccupied metal 3d orbitals. Relative to FeCO, the π^* decreased by ~1.5 eV (Figure 6), compared to a 2 eV decrease in the VBCI simulations. By changing the ligand from CO to NO, the π^* manifold decreases in energy, consistent with the trend found for the MLCT mixing and increasing backbonding through VBCI modeling (Table 3). Importantly, like the VBCI modeling, the BP86 functional also gives an electronic structure description of Fe^{III}−NO(neutral), with strong donation from the Fe into the NO, but unpolarized (calculations were done unrestricted and with polarized initial guesses, but converged to the unpolarized results) and not localized in any particular orbital (this would converge to a low-spin Fe^{III}−$NO^{\bullet}$ description).

While the unpolarized Fe^{III}−NO(neutral) electronic structure is consistent with the data, the polarized, antiferromagnetically coupled Fe^{III}−$NO^{\bullet}$ electronic structure is interesting to consider, due to its similarity to the postulated polarized, antiferromagnetically coupled Fe^{III}−O_2^- electronic structure in the $S = 0$ $\{FeO_2\}^8$ site of oxyhemoglobin.[4] To further explore factors that would lead to an Fe^{III}−$NO^{\bullet}$ electronic structure, calculations were done by increasing exact exchange using the B3LYP functional and a functional mixing BP86 with 40% Hartree−Fock (40% HF). Both the B3LYP and 40% HF functionals found spin-polarized $S = 0$ structures that were lower in energy than the spin-unpolarized electronic structure (the ground state in BP86 calculations) by 0.7 and 13.1 kcal/mol, respectively. The differences between the different electronic states are primarily in the backbonding orbitals, and are detailed in Figure 7. The optimized spin-polarized B3LYP structure has a slightly different geometry compared to the crystal structure (Table 4). The Fe−N−O bond angle decreases slightly from 173.1° to 169.0°, and the Fe−NO bond length increases from 1.68 to1.71 Å, with a corresponding

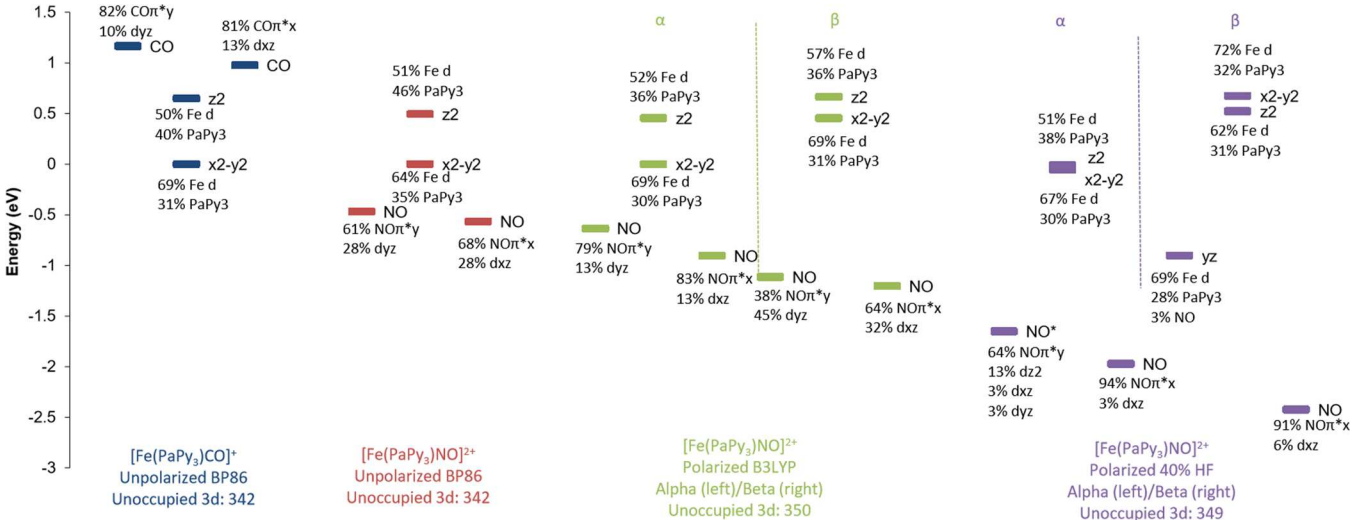

Figure 6. Calculated unoccupied molecular orbital diagrams for $S = 0$ $[Fe(PaPy_3)CO]^+$ and $[Fe(PaPy_3)NO]^{2+}$ using different functionals. All calculations were done in Gaussian 09 with the 6-311G* basis set on the geometry optimized structures. The 40% HF functional is a hybrid functional of BP86 mixed with 40% Hartree−Fock. The B3LYP and 40% HF functionals give polarized electronic structure descriptions, thus separate α and β columns are given for the calculations.

DOI: 10.1021/jacs.6b11260
J. Am. Chem. Soc. 2017, 139, 1215−1225

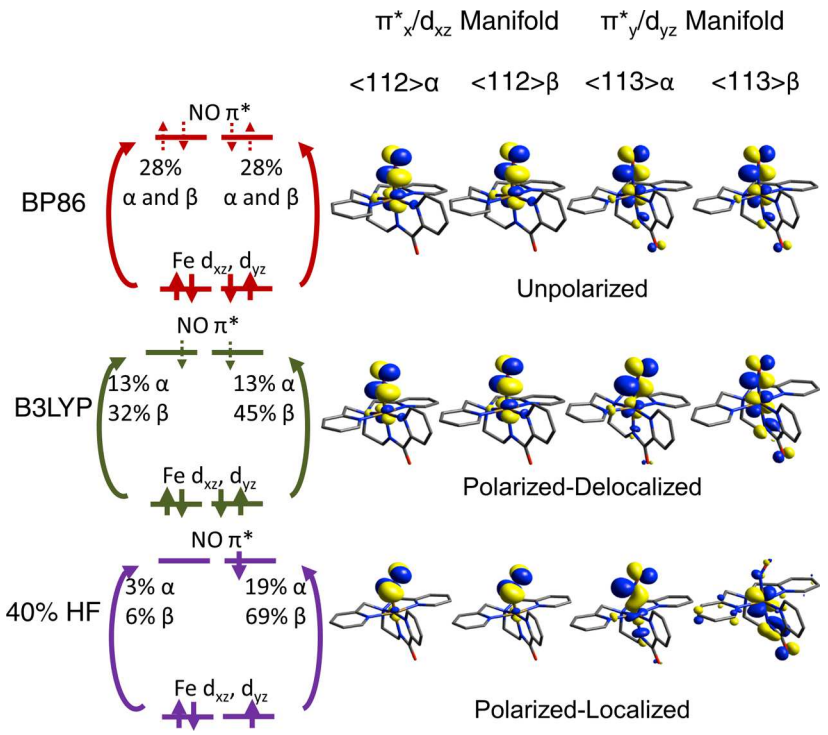

Figure 7. Schematic and contour plots detailing the unoccupied FeNO backbonding orbitals from Figure 6. The BP86 orbitals are from the unpolarized calculation, while the B3LYP and 40% Hartree−Fock orbitals come from the polarized calculations. The percentages in the schematic represent % metal 3d character in the NO π^* orbitals. In the BP86 calculation, there is no spin polarization and the α and β orbitals in each manifold show the same metal 3d character. In the B3LYP calculation, the polarization comes in both manifolds as the β orbital in both π^*_x/d_{xz} and π^*_y/d_{yz} shows greater metal 3d character than in the α orbitals. In the 40% HF calculation, the π^*_x/d_{xz} manifold shows no polarization, while the π^*_y/d_{yz} manifold gives an α hole primarily on the NO and a β hole primarily on the Fe.

decrease in the transaxial bond length from 1.90 to 1.87 Å. In comparing the electronic structures, the total unoccupied d character is roughly the same between the unpolarized BP86 calculation (342% d, second column in Figure 6) and the polarized B3LYP calculation (350% d, green α and β columns in Figure 6). The σ-bonding orbitals are also slightly less covalent in B3LYP compared to BP86. B3LYP calculated 54/57% and 69/69% metal character for the d_{z^2} and $d_{x^2-y^2}$ α/β orbitals, respectively, while as indicated above BP86 gave 51% and 64%, respectively. The largest difference comes in the backbonding orbitals. While the total amount of backbonding was similar between the two (112% in BP86 vs 103% in B3LYP), the spin-polarized B3LYP calculation gave a very different distribution of the metal character across the backbonding orbitals (green α and β columns in Figure 6). Unlike the evenly distributed backbonding with BP86 (2nd column in Figure 6, 28% Fe d in each π^*), B3LYP gave 13/32% and 13/45% metal character in the NO π^*_x and π^*_y α/β orbitals, respectively (Figure 7 middle). This still gives an Fe^{III}−NO(neutral) electronic structure description, since even though the donation into the NO is polarized between the α/β orbitals, it is not localized in a single orbital, as would be reflected in an Fe^{III}−$NO^{\bullet}$ electronic structure (Fe^{III} $S = 1/2$ antiferromagnetically coupled to $NO^{\bullet}$ $S = -1/2$).

With increasing the exact exchange, the optimized geometric structure using the 40% HF functional was extremely different from the crystal structure (Table 4). The Fe−NO bond length increases from 1.68 to 1.99 Å, while the transaxial bond length decreases from 1.90 to 1.79 Å. The Fe−N−O bond angle also decreases from 173.1° to 143.2° (bending into the yz plane). However, the total unoccupied d character of 349 remained similar to the other calculations (purple α and β columns in Figure 6). In the d_{z^2} and $d_{x^2-y^2}$ orbitals, the 40% HF functional gave 51/62% and 67/72% α/β, respectively, which is more spin-polarized but similar in total amount to the values obtained with the other functionals. In the backbonding orbitals, the π^*_x give 3/6% α/β d_{xz} character. However, the π^*_y/d_{yz} manifold polarizes to give a π^*_y α hole with 19% metal d character and a β hole with 69% d_{yz} character (Figure 7 bottom). Thus, with the 40% HF functional, the metal d character is polarized and localized into a single orbital to give the antiferromagnetically coupled Fe^{III}−$NO^{\bullet}$ electronic structure. While the geometry-optimized structure had an Fe−NO bond that elongates and bends, a single point calculation with a fixed, linear Fe−N−O bond angle (173.1°, 1.68 Å) gave the same polarized and localized electronic structure, showing that the change in the electronic structure is not due to the change in the geometric structure.

Overall, the calculations show a trend where increasing exact exchange gives greater polarization and localization of the unoccupied d character in the backbonding orbitals. The BP86 functional gives a completely unpolarized Fe^{III}−NO(neutral) electronic structure, while the B3LYP functional gives a polarized, but delocalized electronic structure, and the 40% HF functional gives a polarized and localized antiferro-coupled Fe^{III}−$NO^{\bullet}$ electronic structure leading to a concomitant change in the geometric structure. The BP86 calculation matches the experimental results best, with very good agreement with the crystal structure distances and angles and the projected VBCI covalencies. The unpolarized BP86 calculation also fits with the experimental L-edge XAS spectrum, which lacks a low energy dπ peak (Figure 2A vs Figure 2D) that would be associated

DOI: 10.1021/jacs.6b11260
J. Am. Chem. Soc. 2017, 139, 1215−1225

with the polarized and localized result obtained with the 40% HF functional.

3.4. Modeling Delocalization vs Antiferromagnetic Coupling. To understand the factors that govern polarization and localization, the model used by Hay, Thibeault, and Hoffman[50] to explain antiferromagnetic coupling in binuclear metal sites was applied to the singlet $\{FeNO\}^6$ system. In the model, the unpolarized description corresponds to a single determinant, and polarization and localization involve mixing of multiple determinants. The singlet $\{FeNO\}^6$ system can be considered as a bonding interaction between a low-spin Fe^{III} with the electron in the metal d_{xz} orbital and an $NO^{\bullet}$ with the electron in the NO π^*_x orbital. The linear combinations of these two orbitals form two orthogonal molecular orbitals (MOs),

$$\varphi_1 = \alpha d_{xz} + \sqrt{1-\alpha^2}\,\pi^*_x$$

$$\varphi_2 = \sqrt{1-\alpha^2}\,\pi^*_x - \alpha d_{xz}$$

where φ_1 is the bonding MO of primarily metal d character and φ_2 is the antibonding MO of primarily NO π^* character. Adding two electrons to these orbitals gives the following singlet electron configurations:

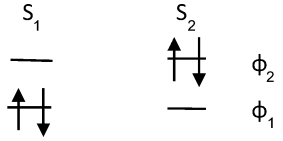

The lowest singlet state Ψ_S can then be expressed as an even contribution of S_1 and S_2:

$$\Psi_S = \lambda_1\Psi_{S_1} + \lambda_2\Psi_{S_2}$$

In the unpolarized limit, $\lambda_1^2 = 1.0$ and $\lambda_2^2 = 0.0$. This gives a fully occupied φ_1 orbital, which is primarily metal 3d character (i.e., Fe^{II}–NO^+). In the antiferromagnetically coupled limit, $\lambda_1^2 = \lambda_2^2 = 0.5$ and the singlet is an equal mixture of S_1 and S_2 (i.e., Fe^{III}–$NO^{\bullet}$). λ_2 thus governs the degree of polarization and its value can be calculated by solving the associated secular determinant, with the result:

$$\lambda_2^2 = \frac{\Delta\varepsilon^2 + 4K_{12}^2 - \Delta\varepsilon\sqrt{\Delta\varepsilon^2 + 4K_{12}^2}}{2(\Delta\varepsilon^2 + 4K_{12}^2)}$$

$\Delta\varepsilon$ represents the energy gap between S_1 and S_2 (that combines both the $\varphi_1 - \varphi_2$ orbital energy difference and the Coulomb repulsion of two electrons in each orbital), and K_{12} represents the exchange interaction between electrons in S_1 and S_2. From the equation, it becomes clear that in the limit $\Delta\varepsilon \gg K_{12}$, $\lambda_2^2 \approx 0$, and in the limit $K_{12} \gg \Delta\varepsilon$, $\lambda_2^2 \approx 0.5$. The degree of polarization is thus governed by these two factors, with a large exchange interaction favoring the antiferromagnetic structure and a large energy gap favoring the unpolarized electronic structure.

The above analysis considers just the single π-bonding interaction between the Fe d_{xz} and NO π^*_x orbitals. However, there is the additional π-bonding interaction between the Fe d_{yz} and NO π^*_y orbitals as well. These two orbitals form the analogous orthogonal MOs,

$$\varphi_3 = \alpha d_{yz} + \sqrt{1-\alpha^2}\,\pi^*_y$$

$$\varphi_4 = \sqrt{1-\alpha^2}\,\pi^*_y - \alpha d_{yz}$$

and the corresponding configurations,

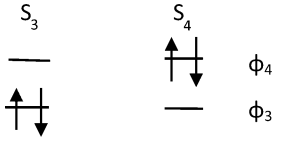

The lowest energy singlet state for $\{FeNO\}^6$ is then expressed by a combination of all four configurations to get

$$\Psi_S = \lambda_1\Psi_{S_1} - \lambda_2\Psi_{S_2} - \lambda_3\Psi_{S_3} + \lambda_4\Psi_{S_4}$$

As in the two orbital system, the values of the λ coefficients govern the polarization of the system. In the unpolarized limit, as described in the BP86 calculation from the previous section, $\lambda_1^2 = \lambda_3^2 = 0.5$ and $\lambda_2^2 = \lambda_4^2 = 0.0$. In the polarized and localized limit, as described in the 40% HF calculation, $\lambda_1^2 = 0.5$, $\lambda_2^2 = 0.0$, and $\lambda_3^2 = \lambda_4^2 = 0.25$. This describes unpolarized bonding in one π manifold and antiferromagnetic coupling in the other π manifold. The polarized and delocalized description, as calculated by B3LYP, has similar degrees of polarization in both manifolds, with $\lambda_1^2 \approx \lambda_3^2 \approx 0.35$ and $\lambda_2^2 \approx \lambda_4^2 \approx 0.15$. The secular determinant that describes this two-bond four electron system is

$$\begin{array}{c|cccc} S_1 & e_{11}+J_{11} & K_{12} & K_{13} & K_{14} \\ S_2 & K_{12} & e_{22}+J_{22} & K_{14} & K_{24} \\ S_3 & K_{13} & K_{14} & e_{11}+J_{11} & K_{12} \\ S_4 & K_{14} & K_{24} & K_{12} & e_{22}+J_{22} \end{array}$$

The off-diagonal matrix elements represent exchange interactions between electrons in the different configurations, while the elements along the diagonal represent the energies of the different configurations which combine the orbital energy and Coulombic interaction of the electrons. The exchange interactions between the configurations are defined in Figure 8.

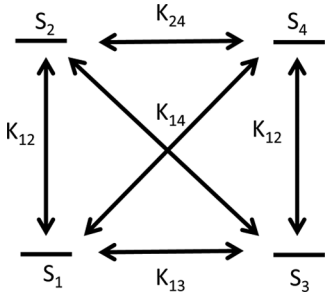

Figure 8. Diagram showing the different exchange interactions between singlet configurations in $\{FeNO\}^6$ π-bonding. S_1 and S_3 represent configurations with filled bonding MOs of mostly Fe d character. S_2 and S_4 represent configurations with filled antibonding MOs of mostly NO π^* character. S_1/S_2 and S_3/S_4 are separate, but equivalent, bonding/antibonding pairs.

As shown in the figure, several assumptions are made to simplify the system. First, electron interactions in φ_1 are assumed to be equivalent to those in φ_3, since these represent orbitals of primarily 3d character that are degenerate in C_{4v} symmetry. By that same reasoning, the electron interactions in φ_2 are assumed to be equivalent to those in φ_4, since those

DOI: 10.1021/jacs.6b11260
J. Am. Chem. Soc. 2017, 139, 1215–1225

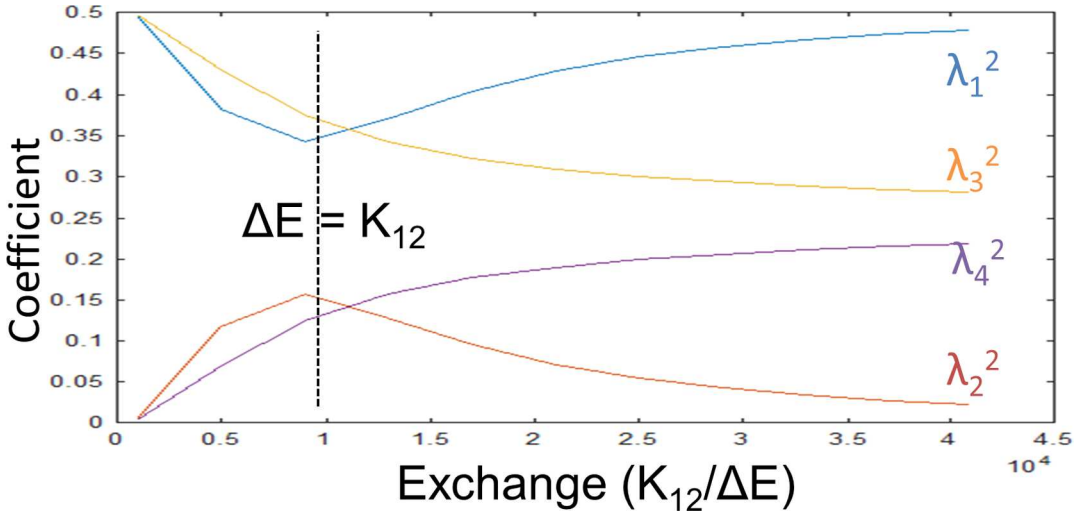

Figure 9. λ^2 coefficients in the wave function $\Psi_S = \lambda_1\Psi_{S1} - \lambda_2\Psi_{S2} - \lambda_3\Psi_{S3} + \lambda_4\Psi_{S4}$ as a function of K_{12} relative to ΔE. As K_{12} increases relative to ΔE, localization of the polarization occurs. In the model, $K_{12} > K_{13} = K_{24} > K_{14}$.

orbitals are degenerate and primarily NO π^* character. These assumptions lead to the above matrix.

Calculating this secular determinant and solving for the λ coefficients gives large expressions that can be evaluated analytically and display important trends in the λ coefficients. The magnitude of the exchange terms should reflect the amount of overlap between the orbitals involved. K_{14}, which represents the interaction between electrons in primarily Fe d_{xz} and NO π^*_y orbitals, would be the smallest since these are localized on different centers and are orthogonal. The K_{13} and K_{24} terms are larger, representing exchange interactions between orthogonal orbitals that are located on the same center, with $K_{13} > K_{24}$ due to exchange on the metal being greater than on the NO. The largest exchange term is K_{12}, which involves the orbitals directly formed through the Fe−NO π-bonding interaction. The amount of overlap and the strength of the π-bonding then govern the magnitude of K_{12}. Aside from the exchange terms, the other relevant variable is the energy gap between S_2 and S_1 (and the equivalent S_3 and S_4), the dependence of which incorporates the orbital energies and Coulombic energies ($\Delta E = e_{11} + J_{11} - (e_{22} + J_{22})$). For the FeNO case, ΔE is positive due to the NO π^* orbitals being higher in energy compared to the Fe 3dπ orbitals.

Figure 9 graphs the λ^2 coefficients with increasing K_{12} relative to ΔE, with nonzero values for K_{13}, K_{24}, and K_{14} (see Figure 8). When $\Delta E \gg K_{12}$, $\lambda_1^2 = \lambda_3^2 = 0.5$ and $\lambda_2^2 = \lambda_4^2 = 0.0$, which gives the unpolarized description for FeNO. As K_{12} increases and is comparable to ΔE, there is polarization along both π-bonding manifolds to give $\lambda_1^2 \approx \lambda_3^2 \approx 0.35$ and $\lambda_2^2 \approx \lambda_4^2 \approx 0.15$, which is the polarized and delocalized description (as in Polarized B3LYP in Figure 6). With $K_{12} \gg \Delta E$, rather than both manifolds continuing to polarize further, only one manifold polarizes while the other becomes unpolarized, with $\lambda_1^2 = 0.5$, $\lambda_2^2 = 0.0$, and $\lambda_3^2 = \lambda_4^2 = 0.25$. This gives the polarized and localized description of an antiferromagnetically coupled Fe^{III}−$NO^{\bullet}$. The localization comes from the small, but nonzero, K_{14} term in Figure 8, the exchange interaction that connects the two π-bonding manifolds into a single system. K_{13} and K_{24}, which also couple the two manifolds, are larger than K_{14} but cancel each other. The trend shown in this analysis explains the DFT calculations, which also found increased polarization and localization with increased exchange.

As shown by the experimental L-edge data in Figure 1A,B and the VBCI analysis in Table 3, the FeCO and FeNO systems have unpolarized electronic structures. From the modeling of the factors that govern polarization and localization, these have $\Delta E \gg K_{12}$ to stay unpolarized. This analysis suggests that to achieve an antiferromagnetically coupled system, the ligand would need to have its π^* orbitals even lower in energy and be an even stronger π-backbonding ligand than NO. Additionally, this analysis shows that polarization localized in one manifold is favored over large polarization across both manifolds due in part to the K_{14} cross-manifold exchange term.

4. DISCUSSION

This study shows the utility of metal L-edge XAS as an experimental probe of highly covalent systems. L-edge XAS provides a direct probe of the unoccupied metal d orbitals, and can be combined with the DOC methodology to quantitatively determine the electronic structure of highly covalent non-innocent metal complexes. Applying this experimental approach to the isoelectronic $S = 0$ FeCO and $\{FeNO\}^6$ compounds shows that FeNO has a much greater amount of π-backbonding compared to FeCO due to the lower energy of its ligand π^* orbitals. This large donation from the iron into the NO ligand effectively leads to an Fe^{III}−NO(neutral) electronic structure, consistent with sulfur K-edge XAS studies on nitrile hydratase[11] and vibrational spectroscopy on $[Fe(TPP)(MI)\text{-}NO]^+$.[23] However, the L-edge spectrum in Figure 2A does not show the dπ hole that would be present in an antiferromagnetically coupled Fe^{III}−$NO^{\bullet}$ as in Figure 2D. The ability to distinguish between these two electronic structures is one of the clear advantages of this L-edge XAS/DOC approach.

DFT calculations and configuration interaction modeling elucidated the factors that govern possible polarization and localization. The DFT calculations showed a shift from an unpolarized Fe^{III}−NO(neutral), to a polarized and delocalized electronic structure, and then to a polarized and localized antiferromagnetically coupled Fe^{III}−$NO^{\bullet}$ electronic structure, as exchange is increased with increased Hartree−Fock mixing. This demonstrates that in the absence of experimental data, DFT calculations alone cannot provide a definitive electronic structure description. The lack of a dπ hole in the L-edge

DOI: 10.1021/jacs.6b11260
J. Am. Chem. Soc. 2017, 139, 1215−1225

spectrum of FeNO provides direct experimental evidence demonstrating the unpolarized DFT electronic structure. In the FeCO and FeNO systems, the Fe 3d orbitals π-backbond with the ligand π^* orbitals to form bonding orbitals of predominantly metal character and antibonding orbitals of predominantly ligand character. From the modeling, the factors most important to polarization are the energy gap between the bonding and antibonding MOs, and the exchange interaction between electrons in the bonding MO with electrons in the corresponding antibonding MO, K_{12} in Figure 8. When the energy gap is large relative to K_{12}, the system remains unpolarized. The spin system gets more polarized as K_{12} increases relative to the energy gap (Figure 9), mirroring the results from the DFT calculations. Additionally, the exchange interaction between electrons in the bonding MOs with electrons in the antibonding MOs in the second manifold, K_{14} in Figure 8, governs the localization seen to the right in Figure 9. As K_{12} increases relative to ΔE, both manifolds polarize. When K_{12} becomes larger than ΔE, the polarization localizes into only one manifold, which is an antiferromagnetically coupled interaction with the other manifold becoming a covalent bond, rather than both manifolds continuing to polarize, which is due to the K_{14} term connecting the diagonal configurations.

This methodology can now be extended to other highly covalent non-innocent systems, in particular $S = 0$ $\{FeO_2\}^8$. The [Fe(pfp)(1-MeIm)O_2] (pfp = picket fence porphyrin) (pfpO_2)$\{FeO_2\}^8$ model system has been studied through L-edge XAS.[29] In that study, the pfpO_2 showed a similar unpolarized electronic structure to the FeNO compound studied here. The DOC analysis of pfpO_2 found that it had only about a third as much total backbonding as FeNO (44% vs 112% d character in the O_2 vs NO π^* orbitals), leading to a Z_{eff} between that of Fe^{II} and Fe^{III}. From the above modeling of FeNO, strong backbonding is required to have a large K_{12}, and therefore a polarized electronic structure. The weaker π-bonding in pfpO_2 explains why it also exhibits an unpolarized electronic structure with no dπ hole in the L-edge XAS. While the pfpO_2 model complex is unpolarized and has a relatively low Z_{eff}, calculations by Shaik et al.[51] on oxy-myoglobin suggested a polarized antiferromagnetically coupled $Fe^{III}-O_2^-$ electronic structure. In contrast to the pfp model compound, the protein has a hydrogen-bond to the distal oxygen of the Fe$-O_2$ site, and this H-bond is thought to be critical in polarizing the Fe$-O_2$ bond. This H-bond could lead to greater backbonding from the Fe to the O_2. A stronger dπ/O_2 π^* backbonding interaction would lead to a larger K_{12} that could overcome ΔE and lead to a polarized electronic structure. This study has shown the utility of L-edge XAS for experimentally defining the bonding in highly covalent systems, and this approach can now be used to experimentally determine the electronic structure of $\{FeO_2\}^8$ sites in heme proteins.

■ ASSOCIATED CONTENT

Supporting Information

The Supporting Information is available free of charge on the ACS Publications website at DOI: 10.1021/jacs.6b11260.

XYZ coordinates and absolute energies of the calculated unpolarized and polarized geometry optimized structures with different functionals for $[Fe(PaPy_3)CO]^+$ and $[Fe(PaPy_3)NO]^{2+}$; comparison of experimental L-edge spectra versus VBCI simulations (PDF)

■ AUTHOR INFORMATION

Corresponding Authors

*pradip@ucsc.edu
*hedman@slac.stanford.edu
*hodgson@slac.stanford.edu
*solomone@stanford.edu

ORCID

James J. Yan: 0000-0001-5516-3446
Pradip K. Mascharak: 0000-0002-7044-944X

Notes

The authors declare no competing financial interest.

■ ACKNOWLEDGMENTS

This research was supported by the National Institute of General Medical Sciences of the National Institutes of Health under award numbers R01GM040392 (E.I.S.) and P41GM103393 (K.O.H), and NSF grants CHE-1360046 (E.I.S.) and CHE-0957251 (P.K.M.). Use of the Stanford Synchrotron Radiation Lightsource, SLAC National Accelerator Laboratory, is supported by the U.S. Department of Energy, Office of Science, Office of Basic Energy Sciences under Contract No. DE-AC02-76SF00515. The SSRL Structural Molecular Biology Program is supported by the DOE Office of Biological and Environmental Research, and by the National Institutes of Health, National Institute of General Medical Sciences (P41GM103393).

■ REFERENCES

(1) Hocking, R. K.; Wasinger, E. C.; Yan, Y.-L.; deGroot, F. M. F.; Walker, F. A.; Hodgson, K. O.; Hedman, B.; Solomon, E. I. *J. Am. Chem. Soc.* **2007**, *129*, 113−125.
(2) Pauling, L.; Coryell, C. D. *Proc. Natl. Acad. Sci. U. S. A.* **1936**, *22*, 210−216.
(3) Pauling, L. *Nature* **1964**, *203*, 182−183.
(4) Weiss, J. J. *Nature* **1964**, *202*, 83−84.
(5) McClure, D. S. *Radiat. Res., Suppl.* **1960**, *2*, 218−242.
(6) Harcourt, R. D. *Int. J. Quantum Chem.* **1971**, *5*, 479−495.
(7) Harcourt, R. D. *Chem. Phys. Lett.* **1990**, *167*, 374−377.
(8) Goddard, W. A.; Olafson, B. D. *Proc. Natl. Acad. Sci. U. S. A.* **1975**, *72*, 2335−2339.
(9) Hunt, A. P.; Lehnert, N. *Acc. Chem. Res.* **2015**, *48*, 2117−2125.
(10) Brown, C. A.; Pavlosky, M. A.; Westre, T. E.; Zhang, Y.; Hedman, B.; Hodgson, K. O.; Solomon, E. I. *J. Am. Chem. Soc.* **1995**, *117*, 715−732.
(11) Dey, A.; Chow, M.; Taniguchi, K.; Lugo-Mas, P.; Davin, S.; Maeda, M.; Kovacs, J. A.; Odaka, M.; Hodgson, K. O.; Hedman, B.; Solomon, E. I. *J. Am. Chem. Soc.* **2006**, *128*, 533−541.
(12) Sun, N.; Liu, L. V.; Dey, A.; Villar-Acevedo, G.; Kovacs, J. A.; Darensbourg, M. Y.; Hodgson, K. O.; Hedman, B.; Solomon, E. I. *Inorg. Chem.* **2011**, *50*, 427−436.
(13) McQuilken, A. C.; Ha, Y.; Sutherlin, K. D.; Siegler, M. A.; Hodgson, K. O.; Hedman, B.; Solomon, E. I.; Jameson, G. N. L.; Goldberg, D. P. *J. Am. Chem. Soc.* **2013**, *135*, 14024−14027.
(14) Enemark, J. H.; Feltham, R. D. *Coord. Chem. Rev.* **1974**, *13*, 339−406.
(15) Daiber, A.; Shoun, H.; Ullrich, V. *J. Inorg. Biochem.* **2005**, *99*, 185−193.
(16) Zhang, L.; Kudo, T.; Takaya, N.; Shoun, H. *Int. Congr. Ser.* **2002**, *1233*, 197−202.
(17) Walker, F. A. *J. Inorg. Biochem.* **2005**, *99*, 216−236.
(18) Brown, C. D.; Neidig, M. L.; Neibergall, M. B.; Lipscomb, J. D.; Solomon, E. I. *J. Am. Chem. Soc.* **2007**, *129*, 7427−7438.
(19) Diebold, A. R.; Brown-Marshall, C. D.; Neidig, M. L.; Brownlee, J. M.; Moran, G. R.; Solomon, E. I. *J. Am. Chem. Soc.* **2011**, *133*, 18148−18160.

DOI: 10.1021/jacs.6b11260
J. Am. Chem. Soc. 2017, 139, 1215−1225

(20) Heilman, B.; Mascharak, P. K. *Phil. Trans. R. Soc. A* **2013**, *371*, 20120368.
(21) Afshar, R. K.; Patra, A. K.; Olmstead, M. M.; Mascharak, P. K. *Inorg. Chem.* **2004**, *43*, 5736−5743.
(22) Patra, A. K.; Rowland, J. M.; Marlin, D. S.; Bill, E.; Olmstead, M. M.; Mascharak, P. K. *Inorg. Chem.* **2003**, *42*, 6812−6823.
(23) Praneeth, V. K. K.; Paulat, F.; Berto, T. C.; George, S. D.; Näther, C.; Sulok, C. D.; Lehnert, N. *J. Am. Chem. Soc.* **2008**, *130*, 15288−15303.
(24) Popescu, V.-C.; Münck, E.; Fox, B. G.; Sanakis, Y.; Cummings, J. G.; Turner, I. M.; Nelson, M. J. *Biochemistry* **2001**, *40*, 7984−7991.
(25) Averill, B. A. *Chem. Rev.* **1996**, *96*, 2951−2964.
(26) Wasser, I. M.; de Vries, S.; Moënne-Loccoz, P.; Schröder, I.; Karlin, K. D. *Chem. Rev.* **2002**, *102*, 1201−1234.
(27) Li, J.; Peng, Q.; Oliver, A. G.; Alp, E. E.; Hu, M. Y.; Zhao, J.; Sage, J. T.; Scheidt, W. R. *J. Am. Chem. Soc.* **2014**, *136*, 18100−18110.
(28) Hocking, R. K.; George, S. D.; Gross, Z.; Walker, F. A.; Hodgson, K. O.; Hedman, B.; Solomon, E. I. *Inorg. Chem.* **2009**, *48*, 1678−1688.
(29) Wilson, S. A.; Kroll, T.; Decreau, R. A.; Hocking, R. K.; Lundberg, M.; Hedman, B.; Hodgson, K. O.; Solomon, E. I. *J. Am. Chem. Soc.* **2013**, *135*, 1124−1136.
(30) Wasinger, E. C.; de Groot, F. M. F.; Hedman, B.; Hodgson, K. O.; Solomon, E. I. *J. Am. Chem. Soc.* **2003**, *125*, 12894−12906.
(31) Hocking, R. K.; Wasinger, E. C.; de Groot, F. M. F.; Hodgson, K. O.; Hedman, B.; Solomon, E. I. *J. Am. Chem. Soc.* **2006**, *128*, 10442−10451.
(32) Hocking, R. K.; DeBeer George, S.; Raymond, K. N.; Hodgson, K. O.; Hedman, B.; Solomon, E. I. *J. Am. Chem. Soc.* **2010**, *132*, 4006−4015.
(33) Afshar, R. K.; Patra, A. K.; Bill, E.; Olmstead, M. M.; Mascharak, P. K. *Inorg. Chem.* **2006**, *45*, 3774−3781.
(34) Yeh, J. J.; Lindau, I. *At. Data Nucl. Data Tables* **1985**, *32*, 1−155.
(35) Thole, B. T.; van der Laan, G.; Fuggle, J. C.; Sawatzky, G. A.; Karnatak, R. C.; Esteva, J. M. *Phys. Rev. B: Condens. Matter Mater. Phys.* **1985**, *32*, 5107−5118.
(36) Cowan, R. D. *The theory of atomic structure and spectra*; University of California Press: Berkeley, 1981.
(37) Butler, P. H. *Point Group Symmetry: Applications, Methods and Tables*. Plenum Press: New York, 1981.
(38) Arrio, M. A.; Sainctavit, P.; Cartier dit Moulin, C.; Mallah, T.; Verdaguer, M.; Pellegrin, E.; Chen, C. T. *J. Am. Chem. Soc.* **1996**, *118*, 6422−6427.
(39) Laan, G. v. d.; Kirkman, I. W. *J. Phys.: Condens. Matter* **1992**, *4*, 4189.
(40) Arrio, M. A.; Scuiller, A.; Sainctavit, P.; Cartier dit Moulin, C.; Mallah, T.; Verdaguer, M. *J. Am. Chem. Soc.* **1999**, *121*, 6414−6420.
(41) Cartier dit Moulin, C.; Villain, F.; Bleuzen, A.; Arrio, M.-A.; Sainctavit, P.; Lomenech, C.; Escax, V.; Baudelet, F.; Dartyge, E.; Gallet, J.-J.; Verdaguer, M. *J. Am. Chem. Soc.* **2000**, *122*, 6653−6658.
(42) Bianconi, A.; Della Longa, S.; Li, C.; Pompa, M.; Congiu-Castellano, A.; Udron, D.; Flank, A. M.; Lagarde, P. *Phys. Rev. B: Condens. Matter Mater. Phys.* **1991**, *44*, 10126−10138.
(43) de Groot, F. *Coord. Chem. Rev.* **2005**, *249*, 31−63.
(44) Frisch, M. J.; Trucks, G. W.; Schlegel, H. B.; Scuseria, G. E.; Robb, M. A.; Cheeseman, J. R.; Scalmani, G.; Barone, V.; Mennucci, B.; Petersson, G. A.; Nakatsuji, H.; Caricato, M.; Li, X.; Hratchian, H. P.; Izmaylov, A. F.; Bloino, J.; Zheng, G.; Sonnenberg, J. L.; Hada, M.; Ehara, M.; Toyota, K.; Fukuda, R.; Hasegawa, J.; Ishida, M.; Nakajima, T.; Honda, Y.; Kitao, O.; Nakai, H.; Vreven, T.; Montgomery, J. A., Jr.; Peralta, J. E.; Ogliaro, F.; Bearpark, M. J.; Heyd, J.; Brothers, E. N.; Kudin, K. N.; Staroverov, V. N.; Kobayashi, R.; Normand, J.; Raghavachari, K.; Rendell, A. P.; Burant, J. C.; Iyengar, S. S.; Tomasi, J.; Cossi, M.; Rega, N.; Millam, N. J.; Klene, M.; Knox, J. E.; Cross, J. B.; Bakken, V.; Adamo, C.; Jaramillo, J.; Gomperts, R.; Stratmann, R. E.; Yazyev, O.; Austin, A. J.; Cammi, R.; Pomelli, C.; Ochterski, J. W.; Martin, R. L.; Morokuma, K.; Zakrzewski, V. G.; Voth, G. A.; Salvador, P.; Dannenberg, J. J.; Dapprich, S.; Daniels, A. D.; Farkas, Ö.; Foresman, J. B.; Ortiz, J. V.; Cioslowski, J.; Fox, D. J. *Gaussian 09*; Gaussian, Inc.: Wallingford, CT, 2009.
(45) Becke, A. D. *Phys. Rev. A: At., Mol., Opt. Phys.* **1988**, *38*, 3098−3100.
(46) Perdew, J. P. *Phys. Rev. B: Condens. Matter Mater. Phys.* **1986**, *33*, 8822−8824.
(47) Becke, A. D. *J. Chem. Phys.* **1993**, *98*, 5648.
(48) Lee, C.; Yang, W.; Parr, R. G. *Phys. Rev. B: Condens. Matter Mater. Phys.* **1988**, *37*, 785−789.
(49) Tenderholt, A. L. *QMForge: A Program to Analyze Quantum Chemistry Calculations*, version 2.4.
(50) Hay, P. J.; Thibeault, J. C.; Hoffmann, R. *J. Am. Chem. Soc.* **1975**, *97*, 4884−4899.
(51) Chen, H.; Ikeda-Saito, M.; Shaik, S. *J. Am. Chem. Soc.* **2008**, *130*, 14778−14790.

DOI: 10.1021/jacs.6b11260
J. Am. Chem. Soc. 2017, 139, 1215−1225